

# Fabrication and Characterization of a Flexible FBG-Based Shape Sensor Using Single-Mode Fibers

Samaneh Manavi Roodsari , Sara Freund , Azhar Zam , *Member, IEEE*,  
Georg Rauter , *Member, IEEE*, and Philippe C. Cattin , *Member, IEEE*

**Abstract**—Minimally invasive surgical procedures have become the preferable option, as the recovery period and the risk of infections are significantly lower than traditional surgeries. However, the main challenge in using flexible tools for minimal surgical interventions is the lack of precise feedback on their shape and tip position inside the patient's body. Shape sensors based on fiber Bragg gratings (FBGs) can provide accurate shape information depending on their design. One of the most common configurations in FBG-based shape sensors is to attach three single-mode optical fibers with arrays of FBGs in a triangular fashion around a substrate. Usually, the selected substrates dominate the bending stiffness of the sensor probe, as they have a larger diameter and show less flexibility compared to the optical fibers. Although sensors with this configuration can accurately estimate the shape, they cannot be implemented in flexible endoscopes where large deflections are expected. This paper investigates the shape sensor's performance when using a superelastic substrate with a small diameter instead of a substrate with dominating bending stiffness. A generalized model is also designed for characterizing this type of flexible FBG-based shape sensor. Moreover, we evaluated the sensor in single and multi-bend deformations using two shape reconstruction methods.

**Index Terms**—Minimally invasive surgery, optical fiber shape sensing, sensors for flexible endoscope, fiber Bragg grating (FBG), fiber sensor characterization.

## I. INTRODUCTION

**L**ASER osteotomy, compared to conventional mechanical bone surgery, allows small, functional, and precise cuts

Manuscript received August 9, 2021; revised December 25, 2021; accepted January 18, 2022. Date of publication February 1, 2022; date of current version July 19, 2022. This work was supported by the Werner Siemens Foundation. (*Corresponding author: Samaneh Manavi Roodsari.*)

Samaneh Manavi Roodsari is with the Center for Medical Image Analysis and Navigation (CIAN), Department of Biomedical Engineering, University of Basel, 4123 Allschwil, Switzerland (e-mail: samaneh.manavi@unibas.ch).

Sara Freund and Philippe C. Cattin are with the Center for Medical Image Analysis and Navigation (CIAN), Department of Biomedical Engineering, University of Basel, Switzerland.

Azhar Zam is with the Biomedical Laser and Optics Group (BLOG), Department of Biomedical Engineering, University of Basel, Switzerland.

Georg Rauter is with the Bio-Inspired Robots for Medicine-Laboratory (BIROMED-Lab), Department of Biomedical Engineering, University of Basel, Switzerland.

Digital Object Identifier 10.1109/TBME.2022.3148040

based on pre-operative planning. When laser osteotomy is combined with endoscopy (minimally invasive surgery), the healing process will be accelerated, and the risk of infection and trauma will be reduced for the patient [1], [2]. However, permanent damage may happen to patients if the shape or tip position of the endoscope is not estimated correctly. Many studies were reported in the literature on using different tracking technologies during the surgery [3]–[5]. Still, they all have shortcomings like electromagnetic (EM) sensitivity (EM sensors), limited resolution (ultrasound imaging), low speed (MRI), or require high doses of radiation (X-ray or CT imaging) [6]. FBG-based shape sensors have received considerable attention in recent years. These sensors are easily integrable into medical instruments as they are bio-compatible and have small diameters. Unlike EM sensors, FBG-based shape sensors are not sensitive to the presence of conductive or ferromagnetic materials and are immune to EM disturbances [7]. These advantages make FBG shape sensors ideal candidates for enabling a closed-loop control system when using elastic structures in clinical applications such as catheter navigation, surgical needle tracking, and medical robotic navigation.

Commercially available FBG shape sensors are mainly based on multicore fibers. However, due to the short distance between the sensing elements and the neutral axis (often less than 100  $\mu\text{m}$ ), the sensor can only detect deformations with bending radii below 10 cm [8], and therefore, are limited to the applications where only large deflections are expected. At the same time, the cost of such systems is high [9] due to the optical frequency domain reflectometer (OFDR) used for FBG interrogation [10] and a fan-out device to read out the signal from the cores [11].

Shape sensors made from multiple single-mode fibers are more cost-effective as expensive custom-made fan-out devices are replaced by standard fiber couplers. To create such a bundle, the optical fibers can either be directly glued together [12], embedded in a grooved cylindrical base [6], molded into flexible materials [13], or attached on a cylindrical substrate [7], [14], [15]. Shape sensors based on these different designs present various benefits and drawbacks and are a tradeoff between flexibility and accuracy. For instance, although gluing the optical fibers together is simple and straightforward, the middle area is filled with extra adhesive, which lowers the mechanical flexibility [12] and may increase the thermal sensitivity of the sensor. Moreover,

these sensor structures have a non-circular cross-section with different bending stiffness for each direction, leading to preferred bending angles for the sensor. In embedded FBG arrays, the sensor has a circular cross-section, and therefore, the bending stiffness asymmetry is negligible, and the sensor is mechanically more stable. However, these sensors can only tolerate small tip deflections [6], [16], or curvatures up to  $2.8 \text{ m}^{-1}$  [17] and are mainly used for needle tracking. Molded FBG sensors may improve the sensor's flexibility to detect up to  $90^\circ$  bending [18], but the self-fabrication process is challenging.

Compared to other methods, for optical fibers attached on a cylindrical substrate the maximum reachable curvature of the sensor can be defined based on the stiffness and the diameter of the substrate (usually  $>1 \text{ mm}$ ) [12], [15], [18]–[21]. In our previous work [14], we designed a shape sensor by attaching three single-mode fibers on a wire-braided Polyimide tube with an outer diameter of  $1.05 \text{ mm}$  and Young's modulus of  $24.7 \text{ GPa}$  [7]. This sensor was able to detect small deformations in the curvature level of  $0.7 \text{ m}^{-1}$  with a  $1.4\%$  positioning error per unit length of the sensor. Although this sensor had a triangular cross-section, the Polyimide substrate, which had higher stiffness than the optical fibers, protected the sensor from bending preferences. However, due to the low flexibility of the substrate, the sensor was mainly suitable for detecting small curvatures (below  $2.5 \text{ m}^{-1}$ ).

In this contribution, we present a 3D shape sensor based on three single-mode fibers glued on a superelastic Nitinol wire. The small diameter of the substrate and its superelasticity enable achieving larger curvatures and increase the flexibility of the sensor. In this design, the bending stiffness of the sensor is no longer dominated by the substrate, which affects the angular behavior of the sensor. Therefore, standard calibration methods fail to model the sensor. Here we proposed a new technique to model asymmetric and highly flexible sensors, which improves the shape estimation accuracy in these types of sensors.

## II. FBG-BASED SHAPE SENSOR WORKING PRINCIPLE

FBGs are periodic structures of different refractive indices inside the core of an optical fiber. They show large reflectivity around a specific wavelength, which fulfills the Bragg condition. The narrow reflected signal, known as the Bragg wavelength, is sensitive to environmental perturbations such as temperature variations and mechanical strain [22]. The Bragg wavelength can be calculated by  $2 n_{eff} \Lambda$ , where  $n_{eff}$  is the effective refractive index and  $\Lambda$  is the period length of the grating. As illustrated in Fig. 1, if the FBG is disturbed, the period length of the grating changes and causes shifts in the reflected signal. The relative Bragg wavelength shift changes linearly with respect to the mechanical strain and temperature variations [19]

$$\frac{\Delta\lambda_B}{\lambda_B} = (1 - P_e) \varepsilon + (\alpha_\Lambda + \alpha_n) \Delta T. \quad (1)$$

In this equation,  $\varepsilon$  is the relative longitudinal change in the Bragg grating caused by a mechanical strain, and  $\Delta T$  indicates temperature variations.  $P_e$ ,  $\alpha_\Lambda$ , and  $\alpha_n$  are strain-optic, thermal expansion, and thermo-optic coefficients, respectively. FBG

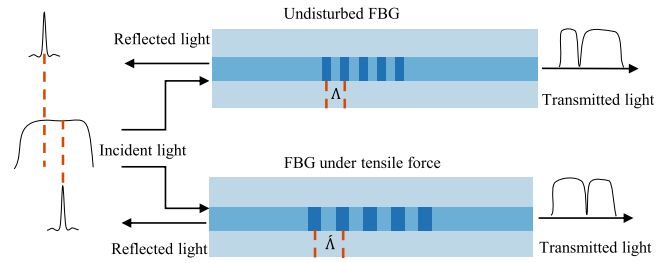


Fig. 1. Working principle of fiber Bragg gratings.

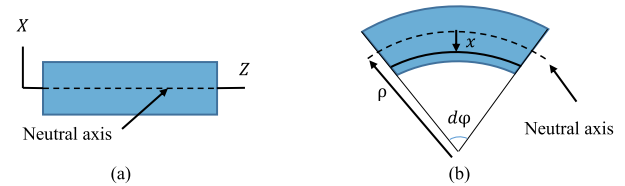


Fig. 2. (a) Bending plane of the beam. (b) Deformation of the beam in pure bending, where  $d\varphi$  is the angle of the selected segment.

sensors can detect bending deflections if placed away from the centroid. In a beam under pure bending (shown in Fig. 2), where the bending moment is constant, the normal strain at a distance  $x$  from the neutral axis (or neutral plane) can be calculated using the following equation [23]

$$\varepsilon_z = \frac{x}{\rho} = k x, \quad (2)$$

where  $\rho$  is the bending radius, and  $k$  is the reciprocal of the bending radius, called curvature. The intensity of the applied force to the beam, called stress, holds the points above the neutral axis in tension, resulting in a positive strain. Points below the neutral axis are under compressive stress, and the strain is negative. In other words, depending on the sign of the strain, the curvature direction can be determined in the bending plane. Therefore, once the normal strain is calculated from the measured wavelength shift in the FBG sensor using (1), the curvature of the beam and the upward or downward direction of bending can be extracted from (2).

Shape sensing using FBGs is based on multiple off-axis strain measurements at the cross-section during bending. At least two FBGs are required to determine the spatial curve of the sensor, assuming that  $z$ -information is already known by the position of the FBGs. A third FBG is further needed to compensate for the effect of temperature on the reflected signal. In the literature, placing three FBGs at each sensor plane was usually done by multicore fibers with FBG arrays [8] or embedded single-mode FBGs in a grooved cylindrical substrate [24]. It was assumed that the sensor probe behaves as a uniform, symmetric, linear Kirchhoff rod [8]. Therefore, considering the sensor probe as a beam under pure bending results in the following equations, which calculate the strain of three independent FBGs (also called FBG triplet) at each sensor plane,

$$\begin{aligned} \varepsilon_1 &= |k| d \sin(\theta) + \varepsilon_T, \\ \varepsilon_2 &= |k| d \sin(\theta + 120^\circ) + \varepsilon_T, \end{aligned}$$

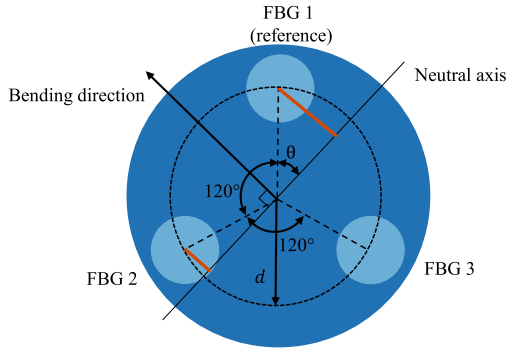


Fig. 3. Cross-section of a shape sensor based on multicore or embedded FBGs. The orange lines indicate the distance between the FBGs and the neutral plane.

$$\varepsilon_3 = |k| d \sin(\theta + 240^\circ) + \varepsilon_T. \quad (3)$$

In these equations,  $d$  is the radial distance between the FBGs and the neutral axis of the sensor, and  $\varepsilon_T$  is the thermal strain. As can be seen in Fig. 3, the sensor probe does not meet the homogeneity condition due to the presence of the optical fibers. However, this heterogeneous material density leads to minor inaccuracies when the sensor is not under tight bending [8].

According to (3), the Bragg wavelength in these sensors changes linearly with respect to curvature and temperature variations. The first arguments on the right-hand side are the normal strain caused by the bending moment in which the distance between the FBGs and the neutral plane (orange lines in Fig. 3) changes sinusoidally depending on the bending direction. Therefore, the sensor's angular behavior can be fitted with a sine function as long as the bending resistance remains the same in all possible directions.

However, attaching the optical fibers to a small cylindrical substrate result in a triangular cross-section with considerable non-uniformity in the material density. Beams with non-uniform bending resistance may twist during bending at specific directions, depending on the shape and density distribution at their cross-section. Therefore, the expression that describes the angular behavior of the sensor should include the effect of twisting at bending directions where material density changes significantly [25]. Consequently, the angular response of the sensor cannot be fitted with a sine wave anymore. Replacing the sine functions in (3) with a general angular function  $G(\theta)$  and substituting it in (1) leads to the following equation system

$$\frac{\Delta\lambda_{Bj}}{\lambda_{Bj}} = F_j (|k|) G_j(\theta) + (\alpha_\Lambda + \alpha_n) \Delta T; \quad (4)$$

$$j = 1, 2, \text{ and } 3.$$

The function  $G(\theta)$  should be obtained experimentally as there are many unknown factors related to the exact shape and density distribution in the cross-section of the fiber bundle after assembling the sensor. Therefore, a calibration setup should be designed such that enough data can be acquired to estimate  $G(\theta)$ . The linear response of the sensor to the curvature variations  $F(|k|)$  is equal to  $\eta(1 - P_e)|k|d_j$  which includes a correction factor  $\eta$  for strain transfer between the substrate and the FBGs.

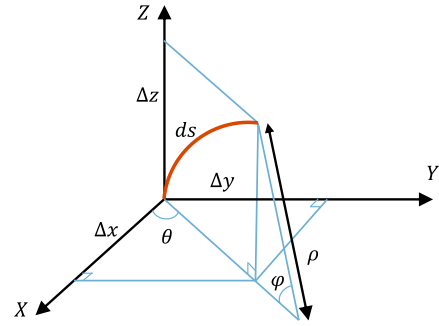


Fig. 4. The local coordinate system for each arc element.

Solving the equation system (4) at each sensor plane provides the curvature and the bending direction, which are later used to reconstruct the 3D shape of the sensor.

### III. 3D SHAPE RECONSTRUCTION

In this paper, we investigated two commonly used methods to reconstruct spatial curves from discrete  $k$  and  $\theta$  values, the kinematic model [26] and Frenet-Serret formulas [24], [8], and compared the predicted shape and tip position of the sensor. For the kinematic model, we first linearly interpolated the measured  $k$  and  $\theta$  to return values at arc elements with 1 mm length along the sensor. Then, each arc element's spatial coordinate was calculated in its local frame using the curvature and bending direction of that segment. Finally, the coordinates of the arc elements were transferred to a global frame to draw the spatial curve of the sensor. As shown in Fig. 4, the local coordinate system for each segment is defined, such that the arc element is tangent to the  $Z$ -axis, and its beginning point coincides with the origin of the frame. Having the bending plane of the arc element at the angle of  $\theta$  from the  $X$ -axis, the homogeneous coordinate of the segment's tip  $P$  can be obtained

$$P = \begin{bmatrix} \Delta x \\ \Delta y \\ \Delta z \\ 1 \end{bmatrix} = \begin{bmatrix} \frac{1}{k} (1 - \cos \varphi) \cos \theta \\ \frac{1}{k} (1 - \cos \varphi) \sin \theta \\ \frac{1}{k} \sin \varphi \\ 1 \end{bmatrix}, \quad (5)$$

where  $\varphi$  is the central angle of the arc, calculated from the curvature multiplied by the arc length  $ds$ ;  $\varphi = k ds$ .

The 3D shape of the sensor is reconstructed by transforming the coordinate of the arc elements from their local coordinate system to the global frame. The global frame  $\Psi_0$  is defined at the base of the sensor, which coincides with the local coordinate system of the first arc element  $\Psi_1$ . Transforming  $\Psi_1$  to the local frame of the second segment includes rotating the coordinate system using  $R_1$  (more detail is available in the Appendix) followed by translation  $T_1$  from  $O_1$  to  $O_2$ , the origins of the coordinate systems

$$T_1 = \begin{bmatrix} 1 & 0 & 0 & -\Delta x_1 \\ 0 & 1 & 0 & -\Delta y_1 \\ 0 & 0 & 1 & -\Delta z_1 \\ 0 & 0 & 0 & 1 \end{bmatrix}. \quad (6)$$

The local coordinate system of the second segment  $\Psi_2$  is as follows

$$\Psi_2 = T_1 R_1 \Psi_1 \quad (7)$$

The transformation matrix from  $\Psi_1$  to the desired local coordinate system  $\Psi_t$ , where  $t$  shows the segment number, is a sequence of the transformation matrices from the previous segments

$$\Psi_t = T_{t-1} R_{t-1} T_{t-2} R_{t-2} \dots T_1 R_1 \Psi_1, \quad (8)$$

which can be reformulated as

$$\Psi_t = R_{t-1} T_{t-1} \Psi_{t-1}. \quad (9)$$

The spatial coordinate of each arc element in the global frame can be calculated by multiplying its local coordinates by the inverse of the transformation matrix

$$\begin{bmatrix} X_{t+1} \\ Y_{t+1} \\ Z_{t+1} \\ 1 \end{bmatrix} = \Psi_t^{-1} \begin{bmatrix} \Delta x_t \\ \Delta y_t \\ \Delta z_t \\ 1 \end{bmatrix}. \quad (10)$$

The second approach to reconstruct the 3D shape of the sensor is based on Frenet-Serret formulas that define the geometric properties of a curve in the Euclidean space. These formulas describe the derivatives of three unit-vectors in terms of each other

$$\begin{aligned} \frac{dt}{ds} &= kn, \\ \frac{dn}{ds} &= -kt + \tau b, \\ \frac{db}{ds} &= -\tau n, \end{aligned} \quad (11)$$

The unit-vector  $t$  is tangent to the curve, the bending direction is shown by the unit-vector  $n$ , and  $b$  is the binormal unit-vector, perpendicular to the bending plane. The torsion, indicated by  $\tau$ , is the derivative of the bending direction  $\theta$  with respect to the arc length  $s$ . Once the unit-vectors at each segment are obtained using the equation system (11), knowing the curvature and the torsion, the position vector  $r(s)$  can be calculated

$$\begin{aligned} dr &= T ds, \\ r(s) &= \int T ds. \end{aligned} \quad (12)$$

Consequently, the spatial coordinate of the segments in the global frame is obtained as a function of the arc length

$$\begin{bmatrix} X(s) \\ Y(s) \\ Z(s) \end{bmatrix} = r(s). \quad (13)$$

#### IV. SENSOR ASSEMBLY AND INTERROGATION SETUP

The performance of the FBG shape sensors using single-mode fibers highly depends on the characteristics of the substrate. In the current design, we replaced the wire-braided Polyimide substrate used in our previous work [14] with a superelastic Nitinol wire that offers higher flexibility and lower thermal sensitivity. The wire's diameter is 0.25 mm, similar to Acrylate

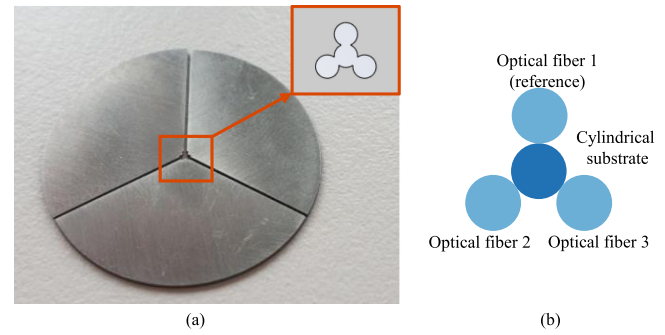


Fig. 5. (a) Three-piece laser cut holder used for aligning the optical fibers on the Nitinol wire. (b) Cross-section of the sensor.

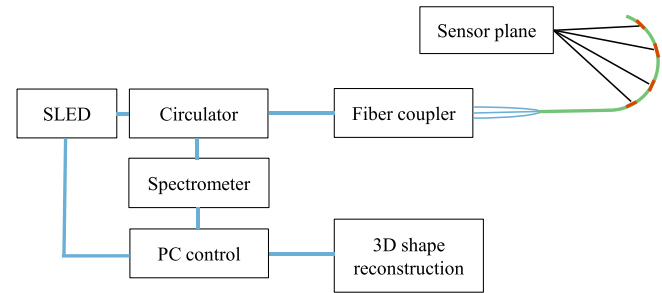


Fig. 6. Schematic of the interrogation setup.

coated optical fibers, making the outer diameter of the sensor 0.75 mm. The single-mode fibers with four FBGs separated by 5 cm were chosen to cover the entire length of a typical 20 cm long endoscope. The three fibers were attached to the substrate using a highly flexible UV-cured glue (LOCTITE AA 3926). Three laser-cut holders were designed to properly align the optical fibers in a 120° configuration on the substrate during the gluing process. Each holder, as shown in Fig. 5(a), was made from three aluminum pieces that create a unique shape in the middle, fitting the triangular cross-section of the sensor (see Fig. 5(b)). The main reason for using multipiece holders was to remove them easily from the fiber bundle once the glue was cured.

The FBGs were interrogated using the wavelength division multiplexing (WDM) technique, as illustrated in Fig. 6. A superluminescent diode (SLED) with an integrated circulator was used to cover the Bragg wavelength of all 12 FBGs from 1515 nm to 1570 nm. The Bragg wavelengths were then monitored using a fast spectrometer (I-MON 512, Ibsen) that was connected to the sensor via a fiber coupler. The measured relative wavelength shifts in the FBG triplets were then used to calculate the spatial coordinate of the arc segment at each sensor plane and to reconstruct the 3D shape of the sensor.

#### V. CALIBRATION

The most common characterization technique for FBG-based shape sensors is to find the calibration curves by monitoring Bragg wavelength shifts in known 3D shapes, which is usually done by rotating the sensor in slots with different curvatures.

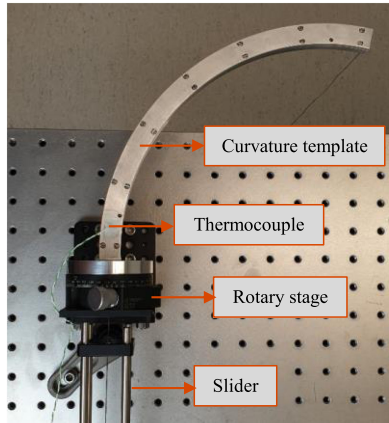


Fig. 7. Calibration setup, curvature template attached to a precision rotary stage.

However, the investigated design has an asymmetrical cross-section with preferred bending directions that causes instabilities during axial rotations. Consequently, repeatable measurements cannot be achieved using calibration setups that include rotational movements. Therefore, we designed 3D curvature templates to acquire ground truth data for bending radii of 17 cm, 20 cm, 23 cm, and 26 cm at all possible directions without the need for rotating the sensor. Each template consisted of a two-piece curved aluminum bar creating a 0.9 mm cylindrical groove in the middle to guide the sensor. The templates were fixed on a precision rotary stage, as shown in Fig. 7, to tune the bending direction accurately. For each curvature, the corresponding template was rotated from 0 to 360°, taking measurements every 20°. After each measurement, the sensor was carefully removed from the template and reinserted in the cylindrical groove at the desired angle using a slider. The Bragg wavelengths were recorded five minutes after sensor insertion for temperature settling, while the temperature was being monitored using a thermocouple attached to the template. Each measurement was repeated three times to reduce random angular deflection during sensor insertion into the template.

Fig. 8(a), (d), and (g) show the measured relative wavelength shifts of the FBGs in the first sensor plane at different bending angles and curvatures. Each data point is an average of three repeated measurements. The sensor warped slightly during bending at directions, where the material resistance varies significantly, resulting in sudden changes in the sensor's output. Therefore, as mentioned in Section II, the sine function describing the angular behavior of the sensor should be replaced with a more general function  $G(\theta)$  that includes the twisting effect during bending. To obtain the function  $G(\theta)$  for each FBG, we first fitted the acquired relative wavelength shifts at different bending angles using a smoothing spline. For the fitted curves to have a continuous transition from 360° to 0° angles and vice versa, we repeated ten data points in the fitting data for bending angles  $\theta < 0^\circ$  and  $\theta > 360^\circ$ , which served as boundary conditions. Then, the normalized versions of the spline fitted curves were averaged to find the angular function  $G(\theta)$  for the three FBGs in the first sensor plane, which are illustrated

TABLE I  
P-VALUES OF ONE-WAY ANOVA TEST ON THE PREDICTION ERROR IN THE CURVATURE AND BENDING DIRECTION AT FOUR FBG TRIPLETS

FBG triplet	1	2	3	4
P-value (Curvature)	0.9805	0.6700	0.3138	0.2459
P-value (Bending direction)	0.4525	0.3794	0.2375	0.2635

in Fig. 8(b), (e), and (h). The function  $F(|k|)$  that predicts the response of each FBG to different curvatures was obtained by linearly fitting the maximum relative wavelength shifts extracted from the spline fitted curves (see Fig. 8(c), (f), and (i)). A similar method was used for all other FBG triplets.

For testing the generality of the proposed model, a 10-fold cross-validation test has been carried out. The data collected from each template were shuffled randomly, then for each fold of cross-validation, 10% of them were left out for evaluation. The remaining data were used to find the function  $G$  and linear fit parameters for co-located FBGs. The estimated values for  $k$  and  $\theta$  were calculated by numerically solving the equation system (4). Table I shows the P-values of the one-way ANOVA test on the curvature and bending direction prediction error for all four FBG triplets. All P-values are higher than 0.05, the significance level, which indicates that differences between the means are not statistically significant. The box plot of the prediction error in curvature and bending direction for different folds at the first FBG triplet is illustrated in Fig. 9, which graphically shows that the median does not significantly change between the folds. Therefore, it can be concluded that the proposed model is general enough to describe asymmetric shape sensors that have bending preferences, and the fitting parameters do not change for different datasets.

## VII. SENSOR EVALUATION

The shape prediction model for the fiber sensor can be selected from any fitting parameters calculated in each fold of the ANOVA test. We tested the sensor's performance, based on fold number 10, in two different situations, single-bend and multi-bend. In single-bend, also known as C-bend, all FBG triplets experienced the same curvature and bending direction, whereas, in multi-bend, various curve deformations existed throughout the sensor.

For the single-bend test, 27 measurements at different curvatures and bending angles were acquired using the 3D templates. Fig. 10(a) illustrates the 3D view of reconstructed shapes using the kinematic model and Frenet-Serret equations, as well as the real shape of the sensor, which is known from the curvature template. The top, side, and front views of all three curves can be seen in Fig. 10(b). The residuals, calculated from the Euclidean distance between the predicted and the real coordinate values at FBG triplet locations, are shown in Fig. 10(c). It can be noticed that the residuals are accumulatively increasing when getting closer to the sensor's tip, which is due to the error in the

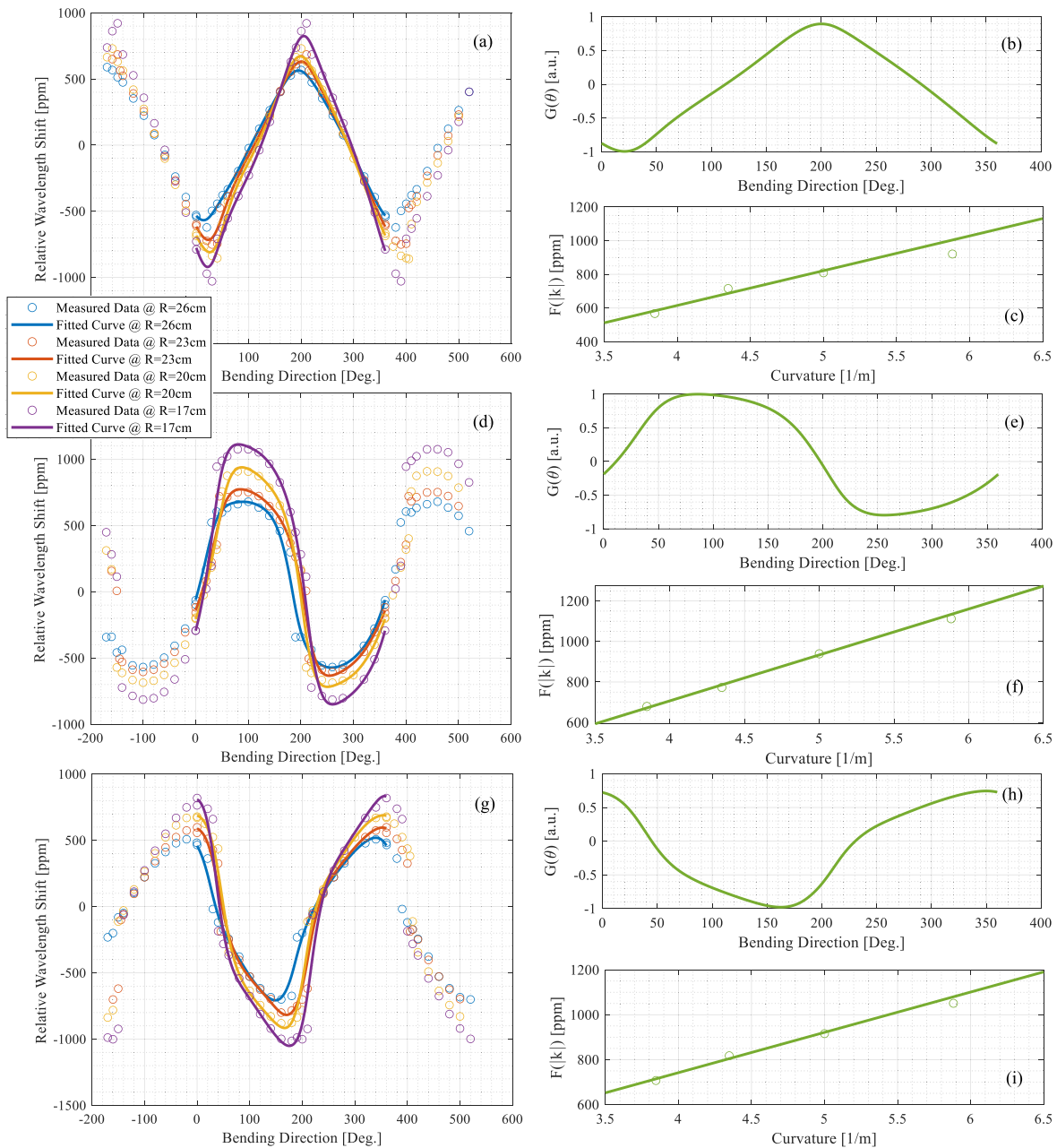


**Fig. 8.** Measured relative wavelength shifts and the fitted curves for the first FBG triplet using four curvature templates (a), (d), and (g). The angular functions are displayed in graphs (b), (e), and (h). The linear functions (also known as curvature sensitivity) for FBG numbers 1, 2, and 3 are shown in figures (c), (f), and (i), respectively.

predicted bending direction. We observed the ascending error in most testing data. In all testing examples, the reconstructed shape using the Frenet-Serret formula had a larger error than the kinematic model. We believe this larger error can be attributed to the adaptive arc elements' length in solving the differential Frenet-Serret equations. The arc lengths in this method depend on how the torsion and curvature values are changing along the spatial curve. The torsion and the curvature values for each arc element are calculated by interpolating predicted  $k$  and  $\theta$  at FBG triplets. Therefore, if the predicted values have an error, interpolating for small elements raises the inaccuracy of the predicted shape even further.

Evaluating the sensor in a multi-bend case, when the sensor experienced larger deflections in arbitrary shapes, was performed using a motion capture system (MOCAP) (Qualisys AB, Sweden). The MOCAP system consists of five cameras to capture motions from different views, as shown in Fig. 11(a). Five passive markers were attached to the sensor to monitor the real shape during data acquisition. The markers are 9.5 mm in diameter and have a 1 mm hole in the middle allowing the fiber sensor to pass through (Fig. 11(b)).

The local coordinate system of the sensor was realized by fixing the sensor's base on a reference plate. The reference plate was a rectangular aluminum part with two circular grooves and

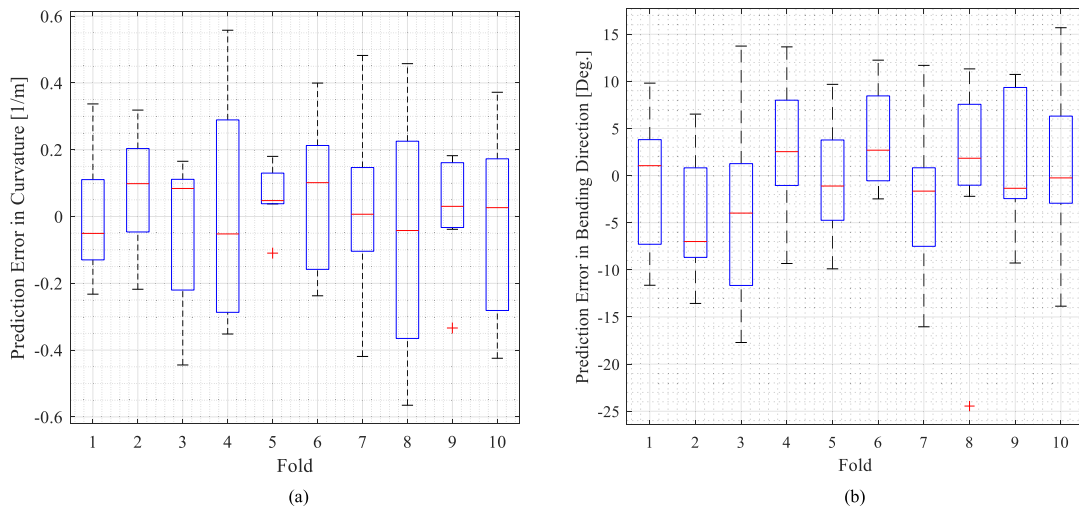


Fig. 9. Box plot of prediction error in (a) curvature and (b) bending direction for 10 folds, at the first sensor plane. On each box, the median is indicated with a central mark, and the 25<sup>th</sup> and 75<sup>th</sup> percentiles are indicated with the bottom and top edges of the box, respectively. The whiskers show the minimum and maximum values within each group not considered outliers, and the outliers are marked with the '+' symbol.

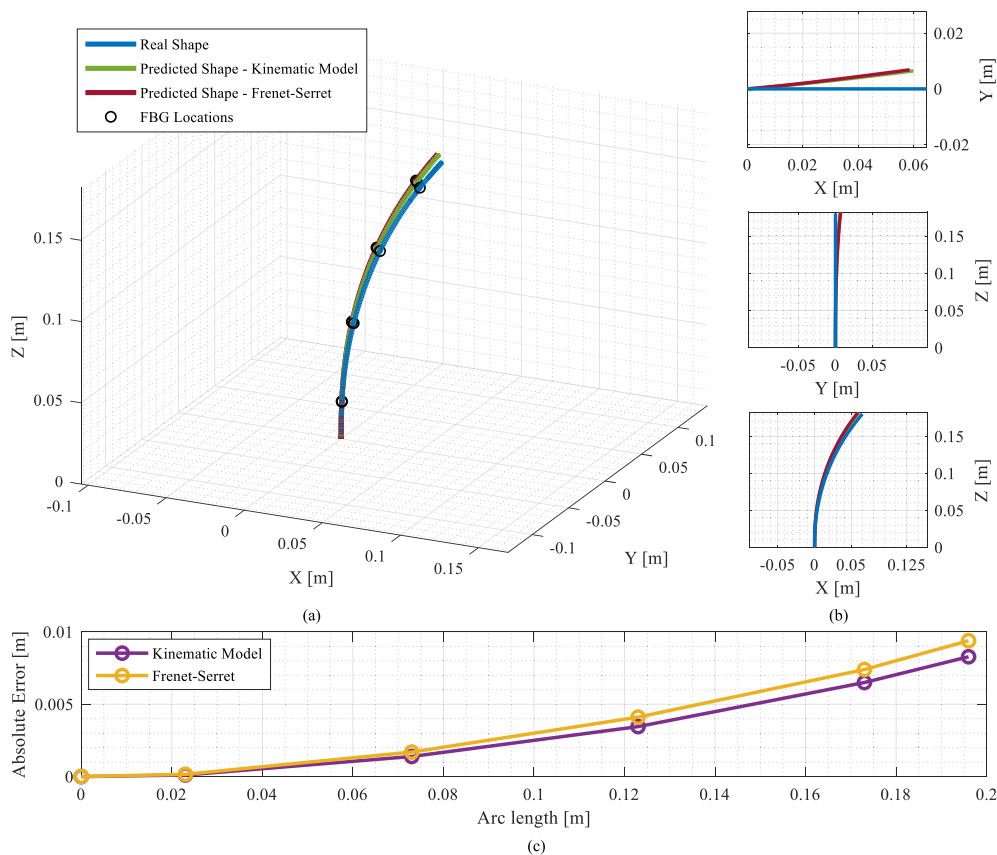


Fig. 10. (a) 3D view, and (b) 2D views of the real and the predicted shapes in a single-bend deformation. (c) The absolute error between the predicted and the real coordinates at FBG triplets, where the circles show the base, the sensing spots, and the tip of the sensor.

one cylindrical groove for placing markers and the sensor in predefined locations. The  $X$  and  $Y$ -axis of the reference plate were measured by placing two markers in the circular grooves and two markers in the cylindrical one, as shown in Fig. 12(a).

The location and orientation of the sensor's base were fixed during data acquisition (Fig. 12(b)). The markers' positions in the coordinate system, defined by the MOCAP managing software, were moved into the sensor's local frame using a

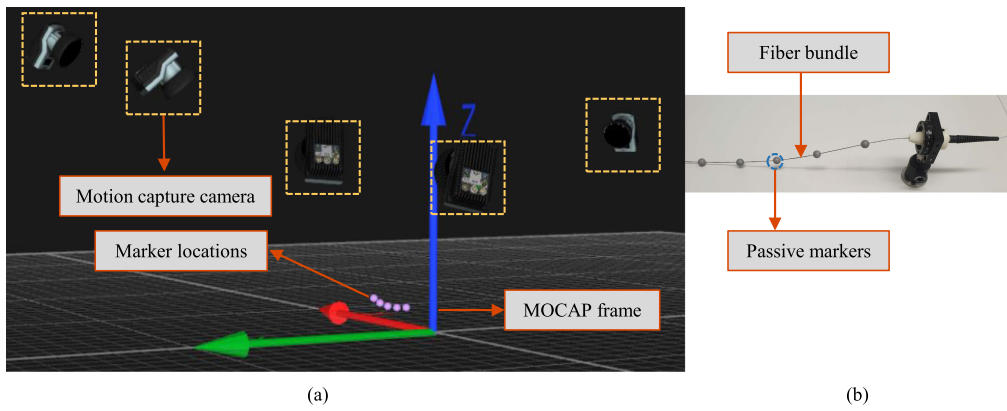


Fig. 11. (a) Oqus camera setup in MOCAP software. (b) Marker attachment to the sensor.

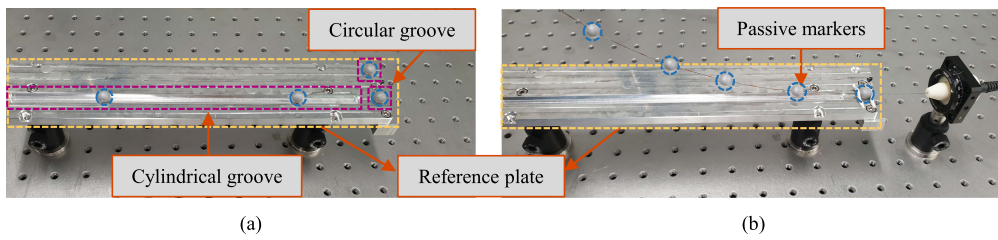


Fig. 12. (a) The local frame realization of the reference plate. (b) Fixation of the sensor in the reference plate.

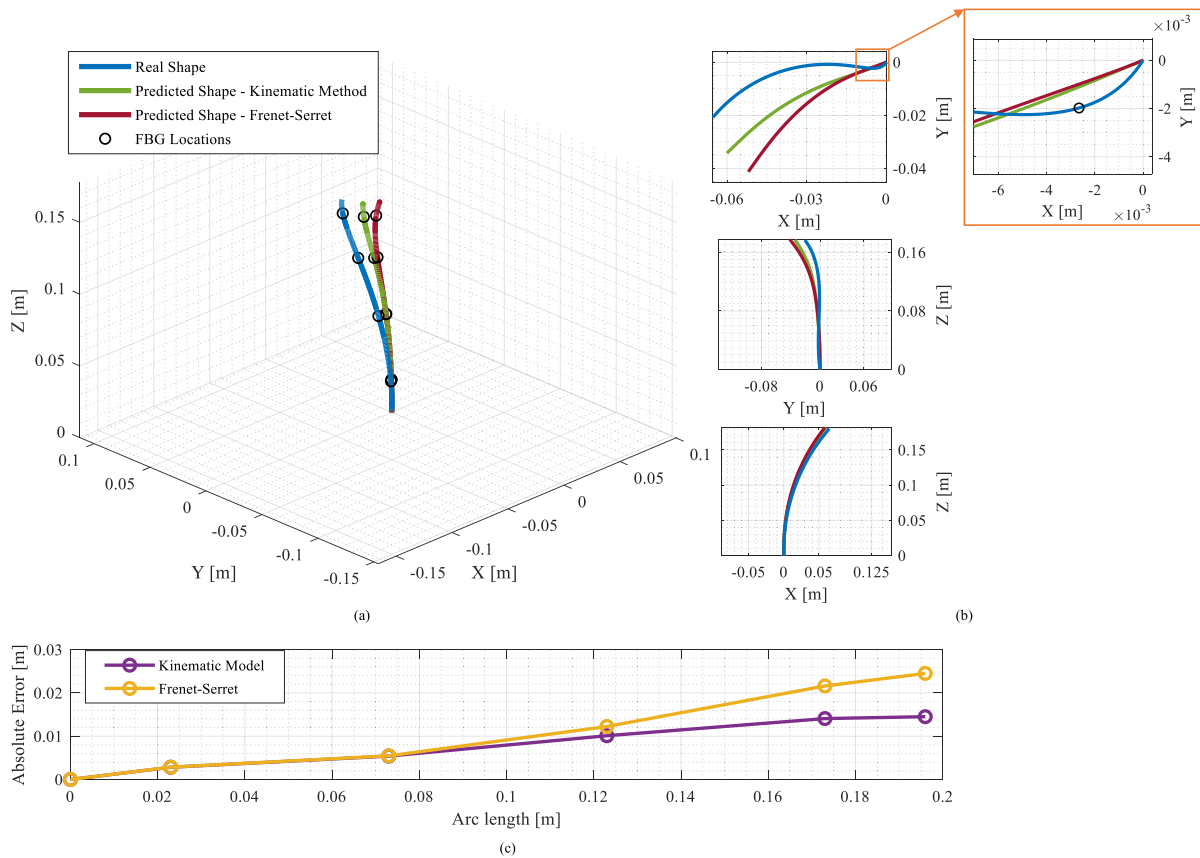


Fig. 13. (a) 3D view, and (b) 2D views of the real and the predicted shapes in a multi-bend deformation. (c) The absolute error between the predicted and the real coordinates at FBG triplets, where the circles show the base, the sensing spots, and the tip of the sensor.

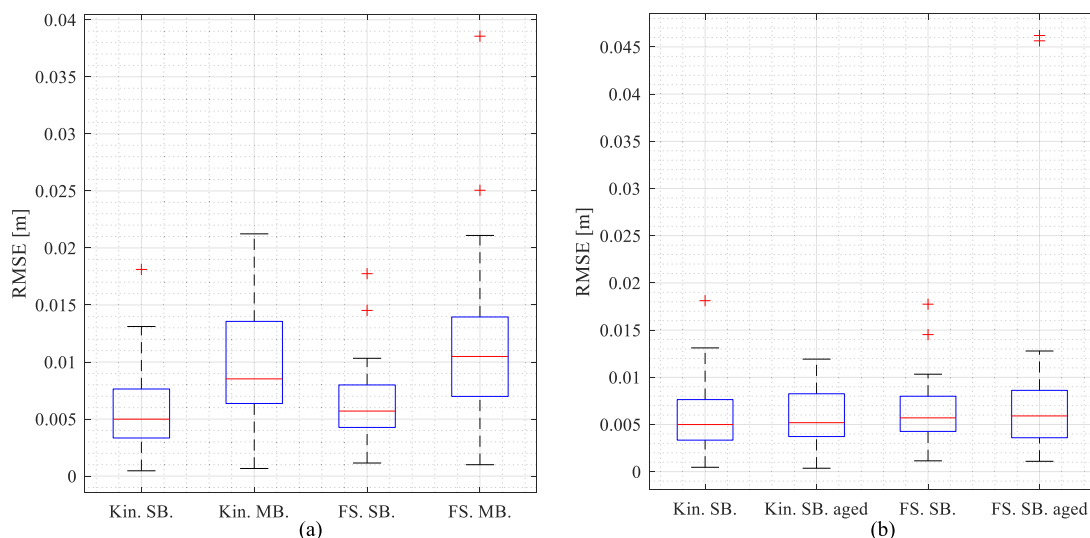


Fig. 14. (a) RMSE of the Euclidean distance between the predicted and real coordinates in single-bend (SB.) and multi-bend (MB.) shapes, reconstructed using kinematic model (Kin.) and Frenet-Serret formula (FS.). (b) The effect of glue aging on the prediction accuracy in single-bend measurements.

transformation matrix. Finally, the spatial curve of the sensor's real shape with 1 mm resolution was estimated by interpolating the marker locations using the cubic spline method [27].

Collecting the testing data in the multi-bend case was performed by moving the sensor's tip at different locations, allowing the sensor to be bent in various curvatures and bending directions from  $0^\circ$  to  $180^\circ$ . The experiment was repeated after rotating the sensor's base for  $180^\circ$  to cover the bending direction from  $180^\circ$  to  $360^\circ$ . To ensure that the tip of the sensor is free to rotate during shape manipulation, it was inserted into a Nitinol tube which was fixed in a moving holder.

An example of the reconstructed shape in the multi-bend experiment is shown in Fig. 13. Similar to the single-bend test, the kinematic model performs better than the Frenet-Serret method. However, as the number of sensing planes was limited, the shape sensor was not able to detect the deformations happening between the sensor planes. In Fig. 13(b), a zoomed view of the beginning part of the sensor in the  $X$ - $Y$  plane is shown. It can be noticed that the sensor did not see the deflection between its base and the first FBG triplet, and therefore, the false prediction in the bending direction resulted in a large error at the sensor's tip. Although this error can also happen in single-bend curves, the shape estimation is still more accurate because the curvature and bending direction are constant in C-bends.

In order to compare the goodness of predicted shapes in single and multi-bend cases, the root mean square (RMS) of the Euclidean distance between the predicted and real coordinates was calculated. The box plot in Fig. 14(a) shows the RMSE for single and multi-bend curves using both kinematic and Frenet-Serret methods. Median values of the RMSE in reconstructed shapes using the kinematic model were 5 mm and 8.5 mm for single and multi-bend, respectively. These values increased up to 5.7 mm and 10.5 mm when Frenet-Serret equations were used for shape reconstruction. The median value for the tip positioning error in single and multi-bend deformations are 9.9 mm and 16.2 mm

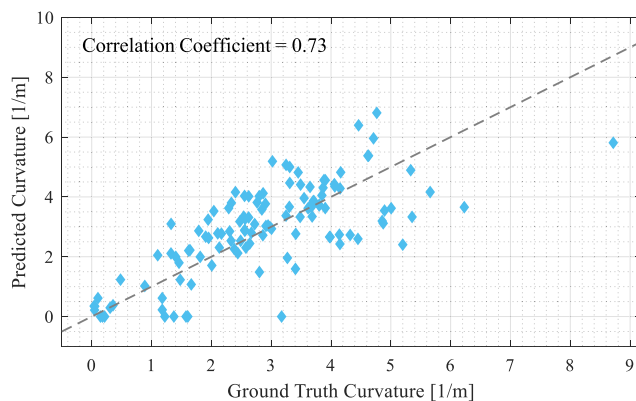
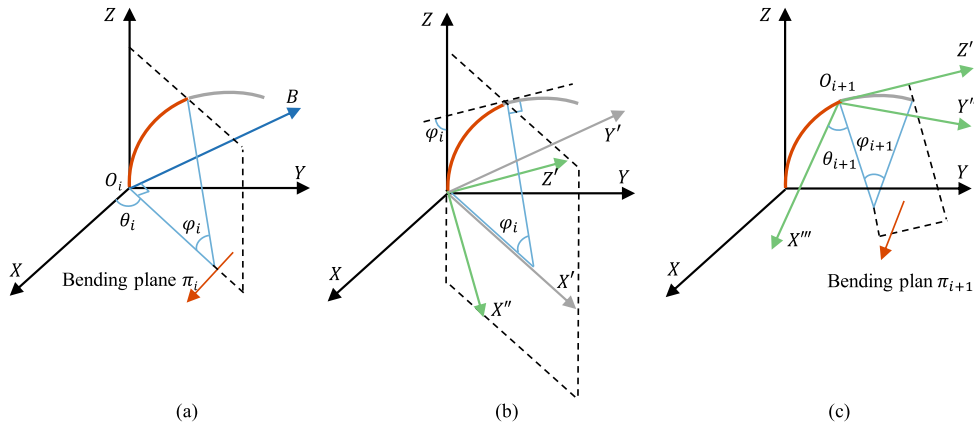


Fig. 15. Scatter plot for the predicted and the ground truth curvatures. The dashed line shows the baseline at  $45^\circ$ .

using the kinematic model, and 12.7 mm and 21.3 mm in the Frenet-Serret method. The higher median values in multi-bend curves, using both kinematic and Frenet-Serret formulas, can be explained by investigating the expected accuracy in marker-based curve estimations. The uncertainty in the estimated marker coordinates and the unknown distance between the centroid of the marker and the sensor's neutral axis are two possible error sources in this method. However, as mentioned earlier, the most important reason is the random twisting effect due to uneven force application during bending or the asymmetric cross-section of the sensor. The latter effect is stronger when the sensor is bent at smaller bending radii.

Another vital parameter to investigate is the bonding strength between the fibers and the substrate, which can be affected by adhesive aging. To study the effect of glue aging on the prediction accuracy, the single-bend measurements were repeated after ten months. As can be seen in Fig. 14(b), the median values of the RMSE were 5 mm and 5.2 mm in kinematic, and 5.7 mm and



**Fig. 16.** The transformation steps from the global frame  $(X, Y, Z)$  to the second local coordinate system  $(X'', Y'', Z')$ . (a) rotation through the angle  $\theta_i$  about  $Z$ -axis, (b) rotation about  $Y'$ -axis through the angle  $\varphi_i$ , (c) rotation about  $Z'$ -axis through the angle  $-\theta_i$  to align the  $X''$ - $Y''$  plane with the bending plane  $\pi_{i+1}$  followed by translation from  $O_i$  to  $O_{i+1}$ .

5.9 mm in Frenet-Serret-based shape reconstructions before and after this period. No significant change in the median value was observed, meaning that the aging of the glue is negligible, and the designed sensor remained stable over this time under the lab condition.

To see how the error changes with respect to the applied curvatures, the scatter plot of the estimated curvatures in the multi-bend experiment is shown in Fig. 15. The correlation coefficient for the predicted and the ground truth curvatures is 0.73, suggesting that the proposed calibration method is indeed suitable for the designed sensor. It can also be noticed that the error increases at higher curvatures, which might be due to the random twisting effect.

### VIII. CONCLUSION

A suitable alternative to EM trackers or multicore fibers in medical tool navigation can be shape sensors composed of three single-mode fibers. In such sensors, the substrate plays a crucial role. If a semi-rigid substrate is used, like Nitinol needles or wire-braided polyimide tubes, an uncertainty of around 1% at the sensor's tip (average error divided by the sensor length) can be reached [6], [14]. However, these sensors are only suitable for applications where small deflections are expected. For a sensor with the same level of flexibility as an optical fiber, a substrate with similar mechanical resistance must be used. Although such a sensor can reach higher curvature levels, bending stiffness at its cross-section is no longer uniform and can show bending preference and random twisting effect during bending. We observed that in such sensor configurations, the prediction accuracy of the bending direction is limited by the random twisting effect, which increases the uncertainty at the sensor's tip up to 5% in medium and 10% in large deflections. Therefore, there is always a tradeoff between the accuracy of the sensor's shape prediction and flexibility. We studied two shape reconstruction methods, the kinematic model and the Frenet-Serret formula. We believe that the kinematic model is more suitable for such sensor design, as it shows higher shape prediction accuracy compared to the Frenet-Serret approach. We also demonstrated that our

sensor shows no significant glue aging after ten months under lab conditions.

For further development of this highly flexible shape sensor, we will use draw tower gratings with polymer coating as they offer higher mechanical strength compared to the currently used stripped FBGs. To compensate for the asymmetric cross-section of the sensor, dummy fibers will be placed around the sensor probe, which may reduce the flexibility of the sensor yet increase the accuracy by limiting bending preferences.

### APPENDIX

Transforming the local frame of the arc element  $i$  ( $\Psi_i$ ) to the local frame of the next segment ( $\Psi_{i+1}$ ) includes rotating the coordinate system about an arbitrary axis called  $B$  through the angle  $\varphi_i$  followed by translation  $T_i$  from  $O_i$  to  $O_{i+1}$ , the origins of the coordinate systems

$$T_i = \begin{bmatrix} 1 & 0 & 0 & -\Delta x_i \\ 0 & 1 & 0 & -\Delta y_i \\ 0 & 0 & 1 & -\Delta z_i \\ 0 & 0 & 0 & 1 \end{bmatrix}. \quad (14)$$

As illustrated in Fig. 16, axis  $B$  is perpendicular to the bending plane  $\pi_i$ , passing through the origin of the frame. A series of rotations are required to obtain the desired orientation of the local frame for the next segment [28]. First, the coordinate system  $\Psi_i$   $(X, Y, Z)$  is rotated through the angle  $\theta_i$  about the  $Z$ -axis, such that axis  $B$  lies in the  $Y$ -axis, aligning the  $X$ - $Z$  plane with the bending plane  $\pi_i$ . The new frame  $(X', Y', Z')$  is then rotated about the  $Y'$ -axis through the angle  $\varphi_i$ , making the  $Z'$ -axis tangent to the tip of the next segment in the  $(X'', Y', Z')$  frame. Finally, step one should be reversed by rotating the  $(X'', Y', Z')$  coordinate system about the  $Z'$ -axis through the angle  $-\theta_i$  to obtain the local frame  $(X'', Y'', Z')$  for the next segment. The total rotation matrix that includes the sequence of rotations is the following

$$R_i = R_{(Z', -\theta_i)} R_{(Y', \varphi_i)} R_{(Z, \theta_i)} \quad (15)$$

where,

$$R_{(Z,\theta_i)} = \begin{bmatrix} \cos \theta_i & \sin \theta_i & 0 & 0 \\ -\sin \theta_i & \cos \theta_i & 0 & 0 \\ 0 & 0 & 1 & 0 \\ 0 & 0 & 0 & 1 \end{bmatrix}, \quad (16)$$

$$R_{(Y',\varphi_i)} = \begin{bmatrix} \cos \varphi_i & 0 & -\sin \varphi_i & 0 \\ 0 & 1 & 0 & 0 \\ \sin \varphi_i & 0 & \cos \varphi_i & 0 \\ 0 & 0 & 0 & 1 \end{bmatrix}, \quad (17)$$

$$R_{(Z',-\theta_i)} = \begin{bmatrix} \cos \theta_i & -\sin \theta_i & 0 & 0 \\ \sin \theta_i & \cos \theta_i & 0 & 0 \\ 0 & 0 & 1 & 0 \\ 0 & 0 & 0 & 1 \end{bmatrix}. \quad (18)$$

## REFERENCES

- [1] "Flagship project MIRACLE | department of biomedical engineering," Accessed: Nov. 12, 2021, [Online]. Available: <https://dbe.unibas.ch/en/research/flagship-project-miracle/>
- [2] M. Eugster *et al.*, "Miniature parallel robot with submillimeter positioning accuracy for minimally invasive laser osteotomy," *Robotica*, vol. 40, pp. 1–28, 2021, doi: [10.1017/S0263574721000990](https://doi.org/10.1017/S0263574721000990).
- [3] C. Shi *et al.*, "Shape sensing techniques for continuum robots in minimally invasive surgery: A survey," *IEEE Trans. Biomed. Eng.*, vol. 64, no. 8, pp. 1665–1678, Aug. 2016, doi: [10.1109/TBME.2016.2622361](https://doi.org/10.1109/TBME.2016.2622361).
- [4] A. Dore *et al.*, "Catheter navigation based on probabilistic fusion of electromagnetic tracking and physically-based simulation," in *Proc. IEEE Int. Conf. Intell. Robots Syst.*, Oct. 2012, pp. 3806–3811, doi: [10.1109/IROS.2012.6386139](https://doi.org/10.1109/IROS.2012.6386139).
- [5] M. Bock *et al.*, "Active catheter tracking using parallel MRI and real-time image reconstruction," *Magn. Reson. Med.*, vol. 55, pp. 1454–1459, May 2006, doi: [10.1002/mrm.20902](https://doi.org/10.1002/mrm.20902).
- [6] R. J. Roesthuis *et al.*, "On using an array of fiber bragg grating sensors for closed-loop control of flexible minimally invasive surgical instruments," in *Proc. IEEE Int. Conf. Intell. Robots Syst.*, Nov. 2013, pp. 2545–2551, doi: [10.1109/IROS.2013.6696715](https://doi.org/10.1109/IROS.2013.6696715).
- [7] S. C. Ryu and P. E. Dupont, "FBG-based shape sensing tubes for continuum robots," in *Proc. IEEE Int. Conf. Robot. Autom.*, May 2014, pp. 3531–3537, doi: [10.1109/ICRA.2014.6907368](https://doi.org/10.1109/ICRA.2014.6907368).
- [8] J. P. Moore and M. D. Rogge, "Shape sensing using multi-core fiber optic cable and parametric curve solutions," *Opt. Exp.*, vol. 20, no. 3, pp. 2967–2973, Jan. 2012, doi: [10.1364/OE.20.002967](https://doi.org/10.1364/OE.20.002967).
- [9] C. Waltermann *et al.*, "Femtosecond laser processing of evanescent field coupled waveguides in single mode glass fibers for optical 3D shape sensing and navigation," in *Proc. SPIE*, May 2015, vol. 9480, pp. 948011–948015, doi: [10.1117/12.2183334](https://doi.org/10.1117/12.2183334).
- [10] B. J. Soller *et al.*, "High resolution optical frequency domain reflectometry for characterization of components and assemblies," *Opt. Exp.*, vol. 13, no. 2, pp. 666–674, 2005, doi: [10.1364/OPEX.13.000666](https://doi.org/10.1364/OPEX.13.000666).
- [11] R. R. Thomson *et al.*, "Ultrafast-laser inscription of a three dimensional fan-out device for multicore fiber coupling applications," *Opt. Exp.*, vol. 15, no. 18, pp. 11691–11697, 2007, doi: [10.1364/OE.15.011691](https://doi.org/10.1364/OE.15.011691).
- [12] M. Cohen *et al.*, *Planar Waveguides and Other Confined Geometries*, New York, NY, USA: Springer, vol. 189, 2015, doi: [10.1007/978-1-4939-1179-0](https://doi.org/10.1007/978-1-4939-1179-0).
- [13] H. Moon *et al.*, "FBG-based polymer-molded shape sensor integrated with minimally invasive surgical robots," in *Proc. IEEE Int. Conf. Robot. Autom.*, May 2015, pp. 1770–1775, doi: [10.1109/ICRA.2015.7139427](https://doi.org/10.1109/ICRA.2015.7139427).
- [14] S. Manavi *et al.*, "Temperature-compensated FBG-based 3D shape sensor using single-mode fibers," in *Proc. Adv. Photon.*, 2018, Paper JTU6C.1, doi: [10.1364/BGPPM.2018.JTU6C.1](https://doi.org/10.1364/BGPPM.2018.JTU6C.1).
- [15] J. Yi *et al.*, "Spatial shape reconstruction using orthogonal fiber bragg grating sensor array," *Mechatronics*, vol. 22, pp. 679–687, Jan. 2012, doi: [10.1016/j.mechatronics.2011.10.005](https://doi.org/10.1016/j.mechatronics.2011.10.005).
- [16] Y.-L. Park *et al.*, "Real-time estimation of 3-D needle shape and deflection for MRI-guided interventions," *IEEE/ASME Trans. Mechatronics*, vol. 15, no. 6, pp. 906–915, Dec. 2010, doi: [10.1109/TMECH.2010.2080360](https://doi.org/10.1109/TMECH.2010.2080360).
- [17] K. R. Henken *et al.*, "Error analysis of FBG-based shape sensors for medical needle tracking," *IEEE/ASME Trans. Mechatronics*, vol. 19, no. 5, pp. 1523–1531, Oct. 2013, doi: [10.1109/TMECH.2013.2287764](https://doi.org/10.1109/TMECH.2013.2287764).
- [18] H. Moon *et al.*, "Fiber-Bragg-grating-based ultrathin shape sensors displaying single-channel sweeping for minimally invasive surgery," *Opt. Lasers Eng.*, vol. 59, pp. 50–55, Aug. 2014, doi: [10.1016/j.optlaseng.2014.03.005](https://doi.org/10.1016/j.optlaseng.2014.03.005).
- [19] A. Othonos *et al.*, "Fibre bragg gratings," in *Wavelength Filters in Fibre Optics*, vol. 123, Germany: Springer Berlin Heidelberg, 2006, p. 197, doi: [10.1007/3-540-31770-8\\_6](https://doi.org/10.1007/3-540-31770-8_6).
- [20] X. Chen *et al.*, "Updated shape sensing algorithm for space curves with FBG sensors," *Opt. Lasers Eng.*, vol. 129, no. April, 2020, Art. no. 106057, doi: [10.1016/j.optlaseng.2020.106057](https://doi.org/10.1016/j.optlaseng.2020.106057).
- [21] B. Kim *et al.*, "Optimizing curvature sensor placement for fast, accurate shape sensing of continuum robots," in *Proc. IEEE Int. Conf. Robot. Autom.*, 2014, pp. 5374–5379, doi: [10.1109/ICRA.2014.6907649](https://doi.org/10.1109/ICRA.2014.6907649).
- [22] S. Yin *et al.*, *Fiber Optic Sensors*, 2nd ed. Boca Raton, FL, USA: CRC Press, 2008.
- [23] J. M. Gere and S. P. Timoshenko, *Mechanics of Materials*. Boston, MA, USA: Springer, 1991, vol. 53, no. 9, doi: [10.1007/978-1-4899-3124-5](https://doi.org/10.1007/978-1-4899-3124-5).
- [24] K. Henken *et al.*, "Accuracy of needle position measurements using fiber bragg gratings," *Minimally Invasive Ther. Allied Technol.*, vol. 21, pp. 408–414, Nov. 2012, doi: [10.3109/13645706.2012.666251](https://doi.org/10.3109/13645706.2012.666251).
- [25] F. B. Seely *et al.*, *The Torsional Effect of Transverse Bending Loads on Channel Beams*. Urbana Champaign, IL, USA: Univ. Illinois, Jul. 1930.
- [26] R. J. Roesthuis *et al.*, "Modeling and steering of a novel actuated-tip needle through a soft-tissue simulant using fiber bragg grating sensors," in *Proc. IEEE Int. Conf. Robot. Autom.*, May 2015, pp. 2283–2289, doi: [10.1109/ICRA.2015.7139502](https://doi.org/10.1109/ICRA.2015.7139502).
- [27] C. de Boor, *A Practical Guide to Splines - Revised Edition*, 1st ed.. New York, NY, USA: Springer 1978.
- [28] M. Duncan, *Applied Geometry for Computer Graphics and CAD*. London, U.K.: Springer, 2005, doi: [10.1007/b138823](https://doi.org/10.1007/b138823).